Journal of Power Sources 364 (2017) 437–448

Contents lists available at ScienceDirect

Journal of Power Sources

journal homepage: www.elsevier.com/locate/jpowsour

Unraveling micro- and nanoscale degradation processes during operation of high-temperature polymer-electrolyte-membrane fuel cells

K. Hengge [a], C. Heinzl [b], M. Perchthaler [b], D. Varley [a], T. Lochner [b], C. Scheu [a, c, *]

[a] Max-Planck-Institut für Eisenforschung GmbH, Max-Planck-Str. 1, 40237 Düsseldorf, Germany
[b] Elcore GmbH, Bayerwaldstr. 3, 81737 Munich, Germany
[c] Materials Analytics, RWTH Aachen University, Kopernikusstr. 10, 52074 Aachen, Germany

HIGHLIGHTS

- Degradation mechanisms in high-temperature polymer-electrolyte-membrane fuel cells.
- Operation related micro- and nanoscale investigation of anodic Pt/Ru catalyst.
- Band of Pt and Ru nanoparticles occurs adjacent to the cathode catalyst layer.
- In-depth TEM and STEM analysis of catalyst dissolution and diffusion behavior.

GRAPHICAL ABSTRACT

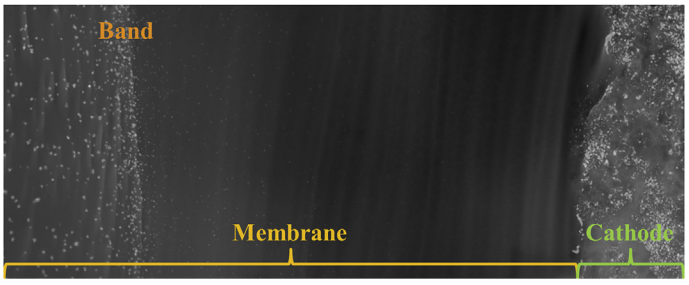

ARTICLE INFO

Article history:
Received 22 February 2017
Received in revised form
1 August 2017
Accepted 11 August 2017
Available online 29 August 2017

Keywords:
High-temperature polymer-electrolyte-membrane fuel cells
Pt/Ru catalyst
Catalyst diffusion
Band in the membrane
Transmission electron microscopy

ABSTRACT

The work in hand presents an electron microscopy based in-depth study of micro- and nanoscale degradation processes that take place during the operation of high-temperature polymer-electrolyte-membrane fuel cells (HT-PEMFCs). Carbon supported Pt particles were used as cathodic catalyst material and the bimetallic, carbon supported Pt/Ru system was applied as anode. As membrane, cross-linked polybenzimidazole was used. Scanning electron microscopy analysis of cross-sections of as-prepared and long-term operated membrane-electrode-assemblies revealed insight into micrometer scale degradation processes: operation-caused catalyst redistribution and thinning of the membrane and electrodes. Transmission electron microscopy investigations were performed to unravel the nanometer scale phenomena: a band of Pt and Pt/Ru nanoparticles was detected in the membrane adjacent to the cathode catalyst layer. Quantification of the elemental composition of several individual nanoparticles and the overall band area revealed that they stem from both anode and cathode catalyst layers. The results presented do not demonstrate any catastrophic failure but rather intermediate states during fuel cell operation and indications to proceed with targeted HT-PEMFC optimization.

1. Introduction

Long-term stability and performance continuity as well as affordable costs are key factors to give fuel cells their final breakthrough in our daily life. Extensive research and development have

* Corresponding author. Max-Planck-Institut für Eisenforschung GmbH, Max-Planck-Str. 1, 40237 Düsseldorf, Germany.
E-mail address: scheu@mpie.de (C. Scheu).

http://dx.doi.org/10.1016/j.jpowsour.2017.08.042

a visible impact, yet there is room for improvement. In polymer-electrolyte-membrane fuel cells (PEMFCs), the catalyst performance and stability in the electrochemical environment during operation has been and is still among the most frequently addressed issues in terms of fuel cell optimization. Catalyst diffusion, agglomeration, dissolution and Ostwald ripening are the most commonly known phenomena of catalyst degradation, but also CO tolerance of the anode catalyst of PEMFCs has been the focus of many research activities. Several CO poisoning mechanisms on the surface of Pt have been reported and reviewed by Lopes et al. [1] Two types of free Pt site adsorption mechanisms are proposed: a linear and a bridge-type adsorption. Both mechanisms result in a positive shift of the reversible potential so the desorption process of CO from the surface of the Pt nanoparticles becomes difficult. The poisoning effect of CO can be overcome by either reducing the CO adsorption or enhancing the CO oxidation or reduction. To accomplish these requirements, several binary, ternary or even quaternary electrocatalysts are under investigation. A selection of elements used in combination with Pt are: Ce [2], Co [2], Fe [2,3], Ni [2], Mo [2], Os [2,4], Pb [2], Rh [2,4], Ru [2,3,5–7], Sn [2,4] and W [2,4]. Ternary or quaternary alloys are usually made by combining Pt with two or three of the aforementioned metals. Russel et al. [7] compared the CO and CO_2 tolerance of the Pt-Mo/C system with the Pt-Ru/C system. The authors claim two different mechanisms to be responsible for the decreased CO poisoning effect of the alloys compared to pure, metallic Pt: in the Pt-Mo/C system, the Mo-species, located on the surface of the alloyed NPs, promote the CO tolerance by a turn-over of the Mo(IV/VI) couple while in the Pt-Ru/C system, water activation at Ru sites is responsible for the enhanced CO tolerance. However, according to Lopes et al. [8], this is the case only for high overpotentials at the anode whereas at low overpotentials, an electronic effect of Ru on the Pt 5d-band structure decreases the CO poisoning effect of the system. Even though in terms of CO tolerance the Pt-Mo/C turns out to exceed Pt-Ru/C, the stability of the Mo-containing system during operation is lower [3].

Another fuel cell degradation mechanism involves catalyst nanoparticle dissolution, migration and precipitation in the membrane with ongoing fuel cell operation time. These nanoparticles were quite often found to form a band in the membrane adjacent to the cathode catalyst layer. This phenomenon is well documented in literature for low temperature PEMFCs [9–14]. High potentials at the cathode side are mostly stated to be the reason for Pt dissolution and migration into the membrane, where crossover hydrogen from the anode is supposed to reduce these ions to metallic Pt. Pt dissolution at the anode side was first reported by Xie et al. [15] and further investigated by Kim et al. [13] The authors claim hydrogen shortage at the anode side to be responsible for Pt oxidation and subsequent migration into the membrane. Pt oxidation due to fuel cell operation conditions is unlikely since the anode potential is considerably lower than the Pt redox potential. Rau et al. [16] are, according to their own statement, the first ones to address operation related catalyst migration in HT-PEMFCs. The authors observed a Pt band in the PBI membrane adjacent to the cathode catalyst layer in secondary electron and backscattered electron images taken in the scanning electron microscope (SEM). A detailed analysis of the catalyst distribution on the nanometer scale was not provided.

In the present work, the bimetallic Pt-Ru/C system was used as anode catalyst and deposited on a high surface area (HSAC) carbon support to realize the hydrogen oxidation reaction. For the cathode catalyst layer, Pt nanoparticles were deposited on HSAC to perform the oxygen reduction reaction. Stability issues and degradation behavior of the two catalyst types in the course of continuous HT-PEMFC operation are addressed by use of electron microscopy and electrochemical analysis.

The HT-PEMFCs investigated in this work have been operated in real fuel cell systems and are designed to last for more than 40000 h. To gain insight into the processes that take place on the nanoscale during operation, we stopped the fuel cells prematurely after deliberately chosen time intervals and analyzed the individual components with scanning TEM (STEM). For this reason, the work in hand does not show any catastrophic failure of the investigated HT-PEMFCs. Rather, the MEAs presented are still operational and show intermediate states of the MEAs in the course of ongoing fuel cell operation time.

2. Experimental details

2.1. Synthesis

The fuel cell fabrication procedure starts with the production of the catalyst layers for anode and cathode side. Therefore, Pt and Ru catalyst precursors are deposited onto the carbon based support layers (provided by elcomax GmbH) via an electroless deposition method. The HT-PEM membrane electrode assemblies (MEAs) are manufactured by doping the electrodes, including the catalyst layers, with phosphoric acid and hot pressing them with a cross-linked polybenzimidazole (BPI) based membrane. The membrane was fabricated by stirring *meta*-PBI powder and N,N-dimethylacetamide (Merck) for 3 h at 200 °C under pressure. After adding a solution of bisphenol A diglycidyl ether in DMAc (Sigma Aldrich), the membranes were casted on a carrier foil and dried at 70–100 °C. More details are given by Ossiander et al. [17].

The architecture of the so prepared MEAs is based on layered structures: The centerpiece is the membrane which is composed of the phosphoric acid doped organic polymer polybenzimidazole (PBI). Adjacent to the membrane are the anode and cathode. Both electrodes can be subdivided into 3 layers, which are the catalyst layer (CL), microporous layer (MPL) and gas diffusion layer (GDL). This work mainly focusses on the membrane as well as the catalyst layers on both the anode and cathode side.

2.2. Investigated samples

In Table 1 the three investigated samples are summarized. MEA_t0 is the reference MEA studied before fuel cell operation. MEA_t1 was operated for a deliberately chosen time interval (t1) and MEA_II was operated twice as long (t2). Both MEAs were operated in a continuous operation mode in real fuel cell systems. All three samples are fabricated in the same manner. In this way it is possible to solely study degradation processes that occur with ongoing fuel cell operation time on the micro- and nanometer scale and exclude any influences stemming from different fuel cell preparation and operation procedures.

2.3. Degradation at long term operation under constant load

Long term operation under constant load was conducted at a current density of 0.2 A cm^{-2} at 160 °C in real fuel cell systems. On the anode side, the cells were fueled with reformed natural gas

Table 1
Overview of the three investigated samples (MEA_t0, MEA_t1, MEA_t2) and their operation time.

Sample	Operation time
MEA_t0	Ready-to-use (reference)
MEA_t1	Continuous operation for one time interval (t1)
MEA_t2	Continuous operation for two time intervals (t2)

(stoichiometry 1.25), on the cathode side air was supplied (stoichiometry 2.0).

2.4. Characterization methods

2.4.1. Structural and chemical analysis

2.4.1.1. Scanning electron microscopy (SEM). Scanning electron microscopy analysis was performed to obtain an overview of the quality and the thickness of the components in the investigated MEAs. For sample preparation, rectangular pieces were cut off each of the three single cells with the help of a scalpel. The sample pieces were fixed in clamp mountings with the MEA cross-section facing up. A JEOL JSM 6490 operated at 15 kV was used. Micrographs exhibiting a high Z-contrast were obtained with the help of a backscattered electron (BSE) detector from JEOL. EDX analysis was performed by use of the attached EDAX detector and the EDAX software. EDX quantification was based on the Cliff-Lorimer equation and the Pt-Lα (9.441 keV), Ru-Lα (2.558 keV), Cl-Kα (2.621 keV) and C-Kα (0.277 keV) lines.

2.4.1.2. Focussed ion beam (FIB) microscopy. The preparation of TEM samples was performed by focussed ion beam (FIB) sectioning using the conventional lift-out technique according to Giannuzzi et al. [18]. An FEI Helios NanoLab600 with an integrated SEM was applied. Lamellae with dimensions of 10 μm length, 1 μm width and 8 μm depth were fabricated by removing the surrounding material with the help of gallium (Ga) ions with an acceleration voltage of 30 kV and a beam current of 6.5 nA. The exposed lamellae were transferred and attached to a copper (Cu) grid and then thinned by Ga ions until electron transparency (<100 nm). The Ga beam current was reduced gradually to 47 pA. Final polishing was performed with an acceleration voltage of 5 kV and a beam current of 15 pA.

2.4.1.3. Transmission electron microscopy (TEM). TEM measurements were performed on an FEI 60–300 Titan Themis which was operated at 300 kV and at 60 kV and a JEOL JEM-2200FS operated at 200 kV. The Titan Themis is equipped with a C_s-corrector for the condensor system. STEM imaging was carried out with the attached high-angle annular dark-field (HAADF), ADF and bright field (BF) detectors simultaneously with a convergence angle of 23.8 mrad and a spot size around 1.5 Å (Spot 6) at 300 kV. For elemental analysis, a Super X-EDX detector from Bruker was used. Diffraction analysis was performed on the JEOL TEM with the attached Gatan camera.

2.4.2. Electrochemical analysis

2.4.2.1. Polarization curves. To record polarization curves, a single cell setup with an active area of 50 cm^2 and a serpentine channel flow field structure was chosen. The flow rates of the reactants were controlled using mass flow controllers. The cell temperature was fixed at 160 °C with the help of electrical heating cartridges and the stoichiometries of the fuel were kept constant at 1.25 for synthetic reformate (76% H_2, 1.2% CO and 22.8% CO_2, Westfalen AG) and 2.0 for air, respectively.

2.4.2.2. Electrochemical impedance spectroscopy (EIS). Electrochemical impedance spectra were recorded with a Zahner PP241 power potentiostat (Zahner Elektrik) at 0.2 A/cm^2 in a 50 cm^2 single cell fed with synthetic reformate at a stoichiometry of 1.25 at the anode and with air at a stoichiometry of 2.0 at the cathode. The frequency range was set between 50 mHz and 50 kHZ. The amplitude was set to 10 mV and the results are shown in Nyquist plots.

2.4.2.3. In-situ cyclic voltammetry (CV). Cyclic voltammograms were recorded using a Zahner PP241 (Zahner Elektrik) and a Zahner IM6ex electrochemical workstation. The MEAs were tested in a 50 cm^2 single cell and fed with dry hydrogen on the anode (which was then used as a pseudo-reference electrode) and humidified nitrogen on the cathode. The electrochemical surface area (ECSA) was determined by cycling the cathode 100 times between 0.095 and 1.1 V with 0.1 V/s, followed by an analysis scan with 0.05 V/s. The ECSA was calculated according to Equation (1).

$$\text{ECSA}\ (\text{cm}^2\ \text{mg}^{-1}) = \text{Charge}\ (\mu\text{C}\ \text{cm}^{-2})/[210\ (\mu\text{C}\ \text{cm}^{-2}) \times \text{catalyst loading}\ (\text{mg}\ \text{cm}^{-2})] \quad (1)$$

3. Results

3.1. SEM investigation

SEM overview images of representative cross-sectional areas of the three investigated membrane-electrode-assemblies (MEAs) are displayed in Fig. 1a–c. The membrane, anode and cathode are exemplarily marked in Fig. 1a. The images were acquired using the backscattered electron detector resulting in a high atomic number contrast. Due to the greater amount of Pt at the cathode side and the lower atomic number of Ru at the anode side, the cathode CL appears as the brightest layer in the MEA and can therefore easily be identified. The higher Pt loading at the cathode side is due to the less effectively catalyzed oxygen reduction reaction (ORR) of Pt compared to the hydrogen oxidation reaction (HOR). In all investigated MEAs there are some cracks present in both the anode and cathode CLs originating from the drying process of the electrodes during the MEA fabrication. These cracks are mostly filled by the membrane material which is soft at elevated temperatures of 160 °C and more.

The membrane material shows different surface roughness at anode and cathode side after fuel cell operation. While the PBI surface seems to be smooth at the cathode side, it is rough at the anode side. There are several explanations within the bounds of possibility but none of them are proven so far. One is based on the fact that the phosphoric acid is diluted at the cathode side due to the production of water during fuel cell operation. The lack of phosphoric acid could influence the roughness of the membrane material. Another reason could be catalyst dissolution, diffusion and redeposition in the membrane during fuel cell operation; this takes place in the presented samples and will be addressed in the results part in section 3.3 and discussed in the discussion part in section 4. Also, the ratio of the molar flux of H_2 and O_2 or electric potential across the membrane are possible reasons.

Fig. 1d addresses the thickness changes of the MEA components with ongoing fuel cell operation times. The unit displayed in y-direction and representing the thickness of the MEA components is arbitrary – yet the relative thickness changes of membrane and electrode CLs are comparable among each other. It is also worth mentioning that the intersection with the x-axis does not equal zero. Membrane and cathode CL continuously decrease in thickness. In the case of the anode, the thickness of the CL stays constant within the error range after t1. After t2, the width of the anode CL decreased, analogous to that of the membrane and cathode CL. Fluctuations in the thicknesses of the investigated MEA components are possible and could stem from variance in the fabrication of the MEA. Still, it is obvious that the size reduction of the membrane and the cathode CL is more severe than the anode CL. Nevertheless, the reduction in thickness did not result in catastrophic failure of the MEAs investigated.

When taking a closer look at the membrane area next to the

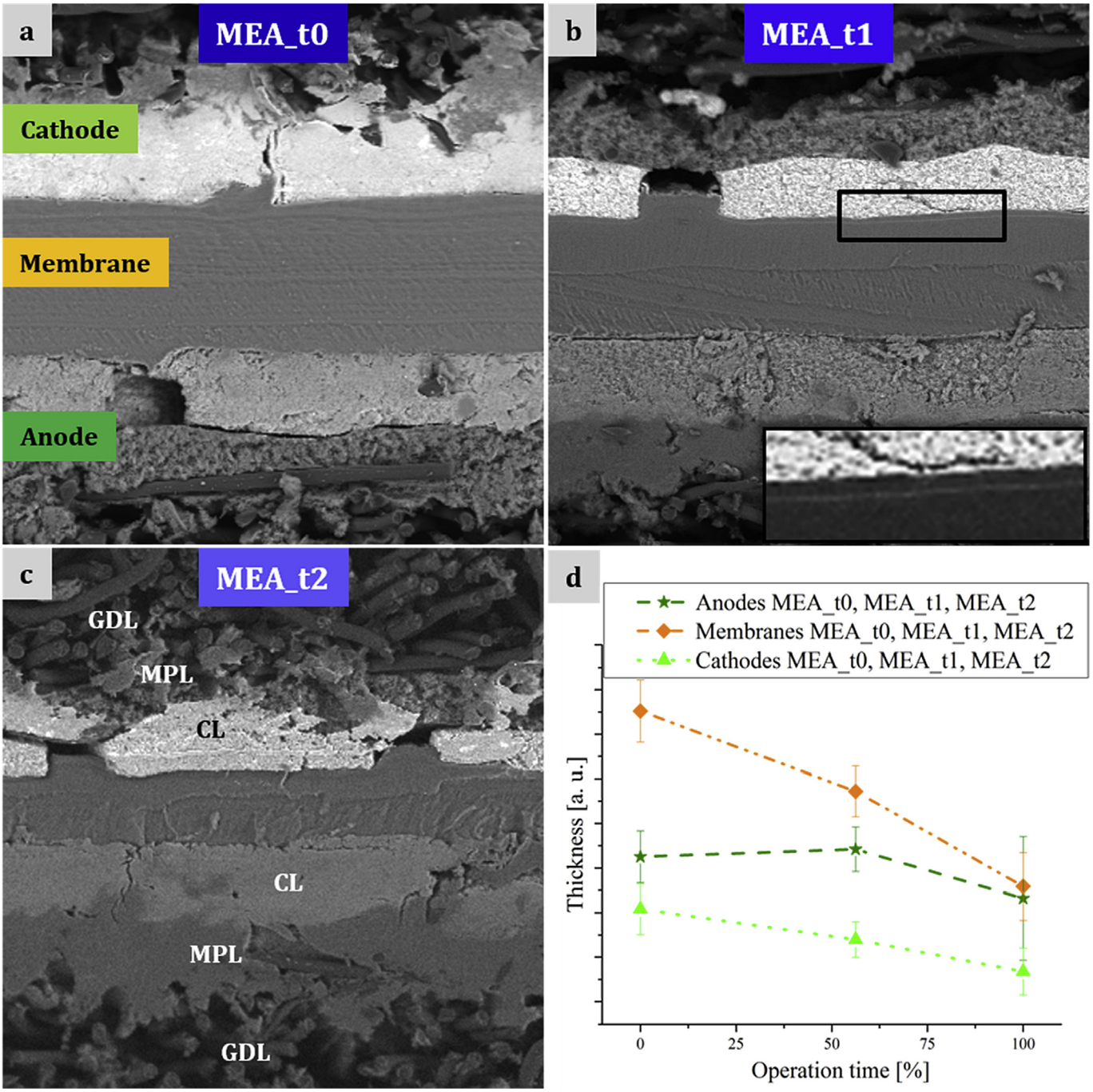

Fig. 1. SEM overview images of the three investigated samples. The layers from top to bottom in each image are: Gas diffusion layer (GDL), microporous layer (MPL), cathode catalyst layer (CL), membrane, anode CL, MPL and GDL: a) MEA_t0 is ready to use; b) MEA_t1 was operated for a certain time interval t1 in continuous FC operation. The inset on the bottom right corner is a magnification of the rectangular marked region between cathode CL and membrane where a bright band is visible in the membrane; c) MEA_t2 was operated for two time intervals in continuous FC operation; d) Operation times of the investigated MEAs are plotted against the mean thickness of MEA components: cathode CL, membrane and anode CL.

cathode CL of MEA_t1, a small band becomes visible (inset in Fig. 1b). Similar observations in HT-PEMFCs after operation have been reported by Rau et al. [16]. In MEA_t2 – after operating the MEA for twice as long – there is no band visible in the SEM image. The reason for this is a combination of the cathode-band distance and the resolution capabilities of the SEM used. The band has moved closer to the cathode and was analyzed in detail by TEM (section 3.3 and in the discussion part in section 4).

Qualitative overview EDX measurements were performed in the SEM on the cross-sections of cathode CL, membrane and anode CL of the three investigated MEAs. The EDX spectra show the presence of C, O, P, Cl, Pt and Ru. Carbon can be found in each functional layer of the investigated MEAs. A HSAC is used as catalyst support at both electrodes and the PBI based membrane is mainly consisting of carbon. Phosphoric acid (H_3PO_4) is used to improve the proton conductivity of the membrane material. Its concentration is highest in the membrane and decreases in direction of both electrodes. A small amount of chlorine (Cl) was detected before fuel cell

operation (MEA_t0) at the cathode side. Obviously, the used Pt precursor was not completely reduced during the fabrication of the MEA. Nevertheless, after the first time interval of fuel cell operation, Cl is removed from the fuel cell and was not detected at later stages. The measured Pt and Ru signals come from the catalyst.

Since the catalyst support on both electrodes is a porous HSAC material, the interaction volume of the electron beam within the sample is large in the SEM. A contribution of adjacent layers to the results of the EDX measurements can neither be excluded nor quantified. For this reason, the results obtained by EDX in the SEM are considered as qualitative results. Nevertheless, even though we know that quantification of carbon has a large error bar due to the low fluorescence quantum yield and absorption in the detector, the amounts of Pt and Ru relative to C were calculated for each of the three investigated MEAs. Carbon corrosion is observed, as discussed above, however, the distribution of carbon is supposed to be more stable than H_3PO_4 and the measurement errors of all investigated samples are assumed to contribute equally to the obtained results. A distinct trend regarding the processes that occur on the μm scale during fuel cell operation is observed: A progressively decreasing amount of Pt and Ru in the anode and also a reducing amount of Pt at the cathode side can be detected by EDX measurements in the SEM. The data can be found in the supplementary Table S1.

3.2. Nanoparticles in the anode-membrane interface region

In Fig. 2, TEM and STEM micrographs of the region comprising the anode CLs and the membranes of MEA_t0 (Fig. 2a), MEA_t1 (Fig. 2d) and MEA_t2 (Fig. 2g) are displayed. As mentioned above, the catalyst used at the anode side is a mixture of Pt and Ru. The presence of Ru leads to conglomerates of individual nanoparticles which are grown together forming polycrystalline, worm-like chains of larger sized particles on the carbon support (Fig. 2b, e, h). Similar clusters of nanoparticles were described by Henry et al. [19] who were facing the same problem as we are in our work: The heavy clustering of the Pt/Ru nanoparticles complicates precise studies of their size, crystallinity and elemental composition before and after fuel cell operation. However, an in-depth investigation of the Pt/Ru catalyst nanoparticles is currently under research and will be addressed in a separate work. Besides being located on the HSAC support, Pt/Ru nanoparticles were also detected in the membrane material close to the anode catalyst layer of MEA_t1 and MEA_t2 but not in MEA_t0. Overview images showing the homogeneous distribution of these particles in the membrane are displayed in supplementary Fig. S1a and b. This confirms what we have already concluded from our SEM analysis: an instability of the Pt/Ru catalyst in the electrochemical environment of the fuel cells during operation leads to catalyst dissolution and diffusion of the Pt and Ru ions into the membrane where they precipitate and form nanoparticles. This process is promoted by the elevated operation temperature of 160 °C present in HT-PEMFCs. The diameters of the catalyst NPs in the membrane close to the anode CL were measured. In MEA_t1, NPs with a mean size of 2.4 ± 0.5 nm were observed (Fig. 2f). With ongoing fuel cell operation time (MEA_t2) two different sizes of the spherical catalyst NPs are present in the membrane: 2.7 ± 0.7 nm and 5.5 ± 0.8 nm (Fig. 2i).

Quantitative EDX analysis was performed in the TEM. A detailed insight into specific areas of the catalyst layers, the membrane and the composition of single catalyst NPs was obtained. The Pt/Ru catalyst particles in the anode catalyst layers are worm-like, about 30 nm long chains, which consist of individual nanoparticles with varying Pt/Ru content. An exemplary Pt/Ru catalyst network is displayed in supplementary Fig. S2, where the amount of Ru locally varies in the range of 19 atom% and 78 atom%; the amount of Pt is vice versa. Although the Pt/Ru catalyst particles contain up to 78 atom% Ru, they still adopt the Pt fcc structure as demonstrated by electron diffraction experiments (see supplementary Fig. S2d). However, the phase diagram [20] would predict a phase separation in Pt fcc and Ru hcp in the presence of high Ru contents. This is most likely another driving force for the observed dissolution.

Overview EDX STEM measurements covering a large area of the anode side reveal a progressively decreasing Ru/Pt ratio with increasing operation time: In the as-prepared state (MEA_t0), 42 ± 4 atom% Ru and 58 ± 4 atom% Pt are present in the anode. After fuel cell operation, MEA_t1 exhibits 38 ± 4 atom% Ru and 62 ± 4 atom% Pt while in MEA_t2 29 ± 4 atom% Ru and 71 ± 4 atom% Pt are found (Table 2). These results indicate a lower stability and thus preferential dissolution of Ru during fuel cell operation compared to Pt. Yet also Pt dissolution is likely to take place (see also Supplementary Table S1).

Quantitative STEM EDX analysis of the nanoparticles in the membrane close to the anode catalyst layer of MEA_t2 was also performed. During the acquisition, the membrane material at the anode side was heavily prone to electron-beam-induced damage. For this reason the EDX acquisition time had to be kept short, thus resulting in higher noise levels and reduced visibility of the particles in the obtained EDX map. The spherical nanoparticles located within the membrane between the anode and the band in MEA_t2 (see supplementary Fig. S1c–e) were found to be composed of 66.2 atom% Pt and 33.8 atom% Ru. This result seems to stand in contrast with the EDX measurements in the anode CL which clearly show that the amount of Ru decreases more rapidly in the anode compared to Pt. TEM investigations can explain this finding as will be shown below in section 3.4.

3.3. Nanoparticles in the cathode

In Fig. 3, STEM micrographs of the interface area between cathode CL and membrane of MEA_t0, MEA_t1 and MEA_t2 are displayed. Compared with the anode side, the catalyst NPs exhibit a spherical shape rather than worm-like chains. The mean size of the Pt catalyst NPs in the cathode CL before fuel cell operation is in the range of 2.0 ± 0.3 nm (Fig. 3b). With ongoing operation time a coarsening of the Pt NPs can be observed which is more severe than at the anode side (Fig. 3). This is due to the harsher conditions at the cathode. After the first time interval of fuel cell operation, the mean diameter of the Pt NPs in the cathode CL is in the range of 5.0 ± 2.3 nm and after the second time interval, the Pt NPs exhibit a size of about 8.0 ± 2.4 nm. These values are listed in Table 3.

The histogram in supplementary Fig. S3 displays the relative number of Pt NPs as a function of their diameter in MEA_t0, MEA_t1 and MEA_t2 in the cathode CL. The measurements are grouped in bins of 0.5 nm. Before fuel cell operation, the sizes of the catalyst NPs vary only in a small range (between 1 nm and 4 nm). With ongoing fuel cell operation time the spread in the size of the catalyst NPs increases. Also, the onsets of MEA_t1 and MEA_t2 are shifted to larger particle size values compared to MEA_t0, proportional to the fuel cell operation times.

3.4. Membrane region with nanoparticle-band

As membrane material, crosslinked polybenzimidazole was used and impregnated with phosphoric acid to improve the material's proton transport ability [21]. STEM measurements of the membrane of MEA_t0 show a constant contrast due to the amorphous structure of PBI (left side of Fig. 3a). Nanoparticles were detected in the membrane after fuel cell operation. Depending on the distance to the cathode CL, two different types of NPs are present in both MEA_t1 and MEA_t2: spherical, monocrystalline

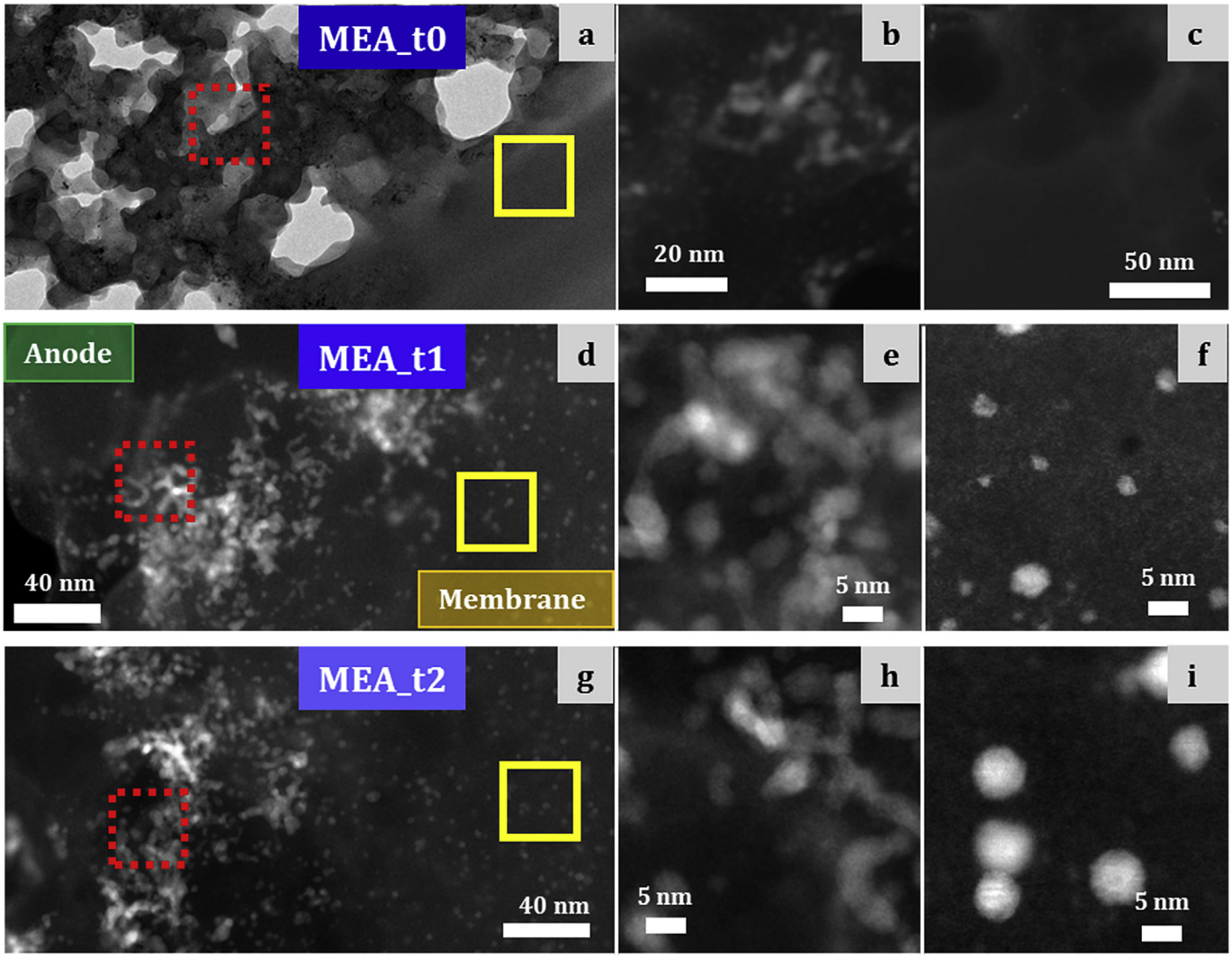

Fig. 2. STEM micrographs of the transition region from the anode catalyst layer to the membrane of a) MEA_t0, d) MEA_t1, g) MEA_t2. b), e) and h) show magnified areas of the anode catalyst layer as marked by dashed, red squares while in c), f), i) high resolution STEM images of the membrane close to the anode and incorporated particles are displayed (marked by yellow squares). (For interpretation of the references to colour in this figure legend, the reader is referred to the web version of this article.)

Table 2
Mean ratio of Ru/Pt in the anode CLs of MEA_t0, MEA_t1 and MEA_t2.

Anode CL	MEA_t0	MEA_t1	MEA_t2
Ru/Pt	0,72 ± 0.11	0,62 ± 0.10	0,42 ± 0.08

NPs with sizes in the range of 2–3 nm are located in the membrane area that is close to the cathode interface (Fig. 3f, supplementary Fig. S4). A large amount of starlike shaped, polycrystalline NPs was detected within the membrane at the band and close to it. In MEA_t1, the average size of these NPs is in the range of 14.7 ± 4.7 nm and in MEA_t2 their mean diameter was found to be 16.1 ± 4.1 nm. These values are displayed in Table 3. Representative STEM micrographs of these NPs are presented in Fig. 3e (MEA_t1) and Fig. 3i (MEA_t2), and also for the case of MEA_t2 in the supplementary Fig. S5. In both operated MEAs, the discussed NPs accumulate to form a band (Fig. 3d and h). In vicinity to this band, the previously mentioned spherical nanoparticles that are observed adjacent to the membrane-cathode interface markedly increase in size (right side in Fig. 3d). The distance between this band and the cathode CL decreases with increasing fuel cell operation time. In MEA_t1, the band is on average 2.3 ± 0.2 μm away from the cathode CL while in MEA_t2, the mean distance was found to be 0.4 ± 0.1 μm. According to the model of Zhang et al. [22], the position of the band in the membrane is determined by the ratio of 2/1 of the molar flux of crossover H_2 and O_2 and the gas permeability of the membrane material [22]. The authors claim that with unchanged permeability characteristics of the membrane, the relative location of the band is independent of the membrane thickness. Zhang et al. also state that in an H_2/air operation condition – which is the case for our fuel cells – the position of the band is expected to be close to the membrane/cathode interface. Our results are in good agreement with these statements. A detailed discussion regarding the degradation behavior of the membrane as well as formation and final position of the band in the electrolyte can be found in the discussion part in section 4.

In Fig. 4 the elemental distribution of Pt and Ru in a representative area of the cathode CL and the membrane of MEA_t2 is displayed. The results of the elemental quantification are summarized in Table 4. The membrane in the displayed micrograph can be subdivided into three regions: the area at the cathode side, the Pt/Ru band and the area in direction of the anode side. Cathode CL

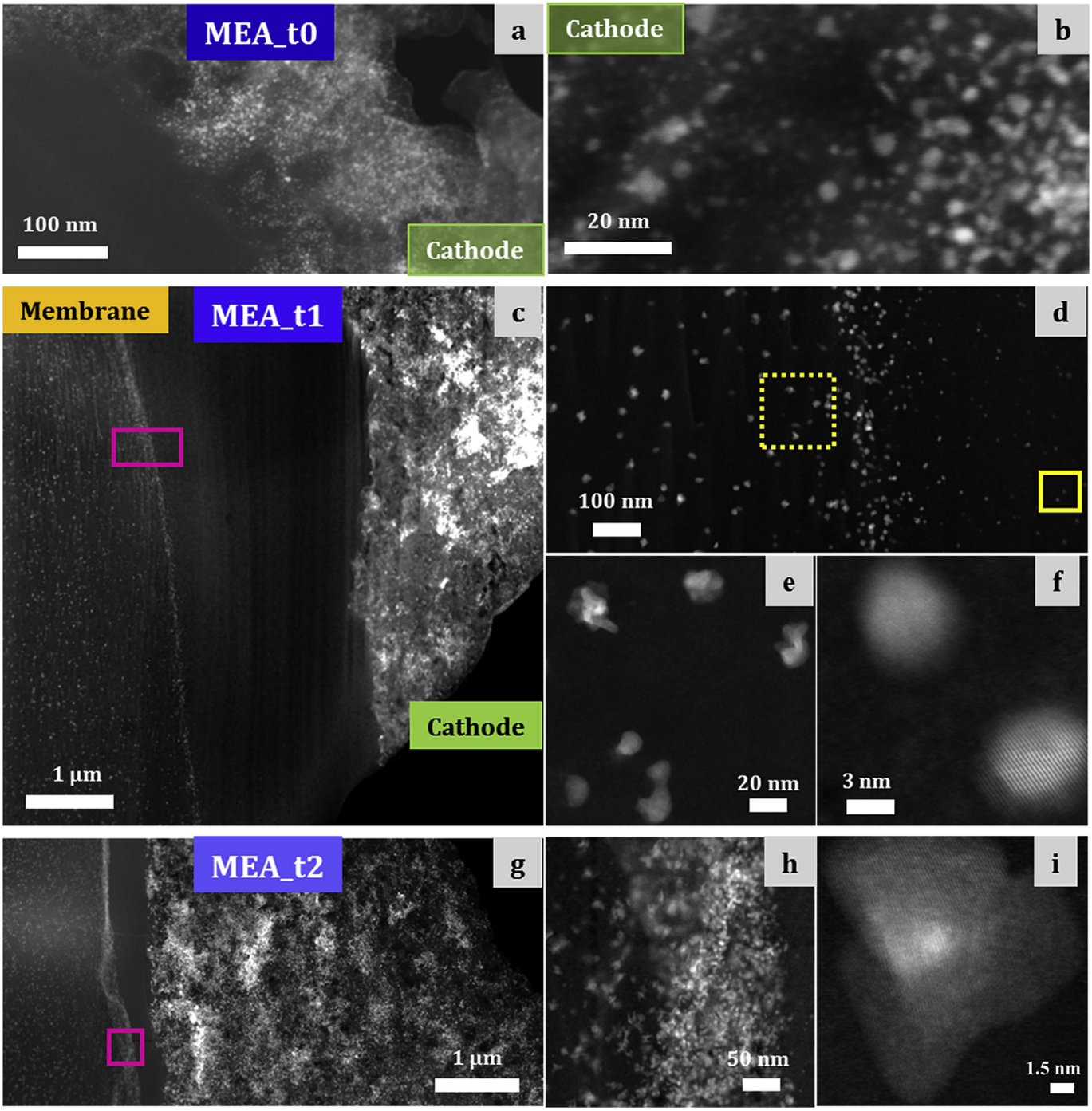

Fig. 3. STEM micrographs of the transition region between membrane and cathode catalyst layer of a) MEA:t0; c) MEA_t1; g) MEA_t2. b) magnified area of the cathode CL of MEA_t0; d) and h) STEM micrographs of the band in the membrane of MEA_t1 and MEA_t2; e), f), i) high resolution STEM micrographs of single particles in the membrane of MEA_t1 and MEA_t2.

Table 3
Mean size distribution of catalyst nanoparticles in the cathode and the adjacent membrane.

	MEA_t0 [nm]	MEA_t1 [nm]	MEA_t2 [nm]
Pt NP in cathode	2.0 ± 0.3	5.0 ± 2.3	8.0 ± 2.4
Pt/Ru NP in membrane adjacent to cathode CL	/	14.7 ± 4.7	16.1 ± 4.1

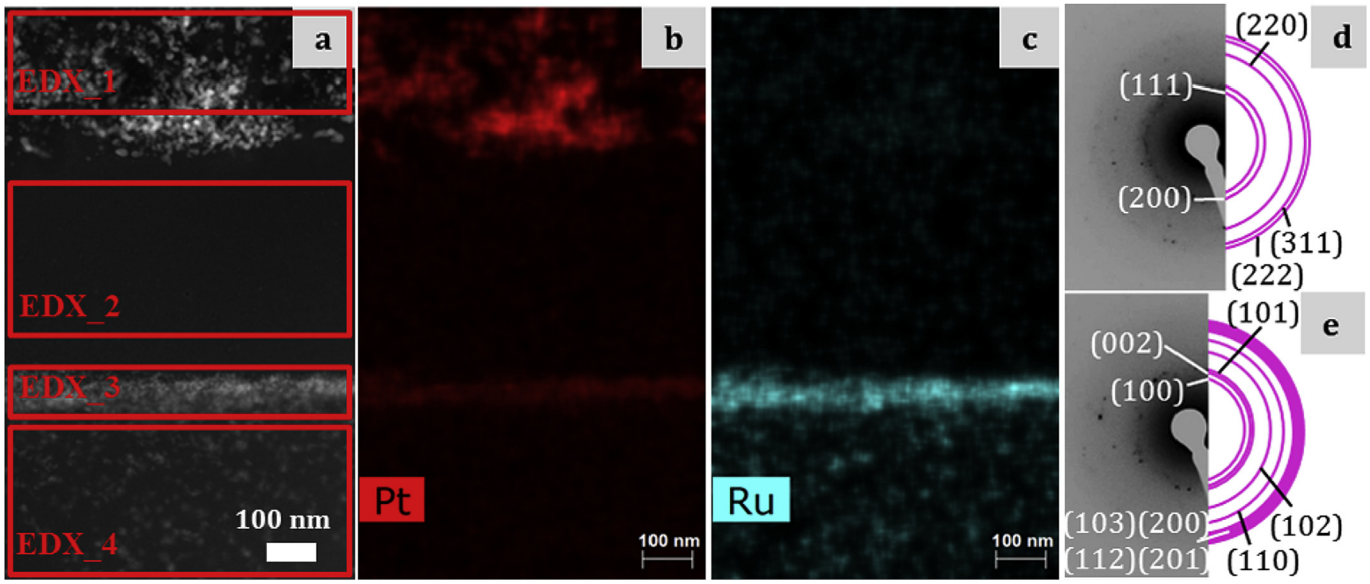

Fig. 4. Elemental distribution of Pt and Ru in the interface region of cathode CL (upper part) and membrane (lower part) of MEA_t2. The distribution of Pt and Ru is marked in red and blue. d), e) Electron diffraction patterns of d) the band and e) several Pt/Ru particles in the membrane area between anode and band. (For interpretation of the references to colour in this figure legend, the reader is referred to the web version of this article.)

Table 4
Pt/Ru ratio in the area shown in Fig. 4.

	EDX_1 Cathode	EDX_2 Membrane	EDX_3 Band	EDX_4 Nanoparticles in membrane
RuL [Atom%]	0	0	62 ± 3	82 ± 4
PtL [Atom%]	100	100	38 ± 3	18 ± 4

(EDX_1) and membrane between the cathode side and the band (EDX_2) are free of Ru. The presence of Pt in the discussed membrane section indicates a small, periodically repeated cathodic Pt catalyst dissolution, migration and precipitation during fuel cell operation. This is confirmed by qualitative SEM EDX analysis (see supplementary Table S1).

The band in the membrane contains 62 atom% Ru and 38 atom% Pt (see Table 4). On average the starlike shaped NPs near the band in direction of the anode side contain 82 atom% Ru and 18 atom% Pt while the spherical Pt/Ru nanoparticles closer to the anode have only ca. 34 atom% Ru (see section 3.2). This suggests that the dissolution and diffusion velocity of Ru are higher than that of Pt. The Pt amount in the band is higher than in the star-like shaped NPs. This is most likely due to Pt stemming from the cathode side. Pt and Ru from the anode side dissolve at elevated fuel cell operation temperatures in the electrochemical environment of HT-PEMFCs. The ions diffuse into the membrane where they are periodically redeposited and dissolved with intermitted diffusion. Similarly the same process happens with Pt in the cathode CL. Thus the catalyst material stemming from both the anode and cathode side is periodically dissolving, diffusing and reprecipitating until it reaches a certain equilibrium point where the molar flux of H_2/O_2 equals 2/1. At this point dissolution, diffusion and precipitation proceed within the band area. Taking all EDX results in the different membrane regions into consideration, ca. 47% of the Pt in the band stems from the cathode catalyst layer and 53% from the anode catalyst layer. The detected Ru is solely coming from the anode side.

Electron diffraction experiments were carried out on several starlike shaped Pt/Ru nanoparticles in the membrane and on the band of MEA_t1 and MEA_t2. All obtained diffraction patterns consist of spots that form circular rings due to the selected area diffraction aperture capturing contributions from several nanoparticles. The diffraction pattern displayed in Fig. 4e is representative for measurements on several starlike shaped nanoparticles in the membrane of MEA_t1; the one shown in Fig. 4d is typical of those obtained from the band. Diffraction analysis revealed that the starlike shaped Pt/Ru particles in the membrane containing a high amount of Ru mainly crystallize in the hcp lattice which is in accordance to the bulk phase diagram. The nanoparticles forming the band were found to crystallize in the Pt fcc lattice due to the lower amount of Ru and the high amount of Pt which is stemming from both anode and cathode CLs. Depending on the amount of Ru and Pt present, the Pt fcc or Ru hcp lattice is adopted.

HRSTEM micrographs reveal different shapes of the catalyst particles in the membrane region between anode and band after the two different operation times (Fig. 5). In the case of MEA_t1 (Fig. 5a–d) the particles exhibit a starlike shape while in MEA_t2, after twice the operation time, the particles are formed by several, randomly overlapping, facetted discs (Fig. 5e–h). This can also be seen nicely in the overview STEM image in the supplementary Fig. S5. EDX maps reveal the elemental distribution of Pt (red) and Ru (blue) within the Pt/Ru nanoparticles in the membranes of the two operated MEAs. In MEA_t1 (Fig. 5d), both elements are distributed uniformly within each of the nanoparticles. This was found to be in contrast to MEA_t2 (Fig. 5h) where Pt seems to gather in one region while Ru is distributed more uniformly. Henry et al. [19] describe in their work that Pt-Ru NPs in the Nafion membrane of low temperature PEMFCs exhibit Pt-core Ru-shell structure. Although this is not the case in MEA_t1, the particles in MEA_t2 might be in an intermediate state before reaching a similar core-shell structure. The average composition of the NPs in MEA_t1 is 71 atom% Ru and 29 atom% Pt, while in MEA_t2 the average amount of Ru was found to be 82 atom%. A detailed analysis of the degradation behavior of the anodic Pt/Ru catalyst in simulated accelerated fuel cell operation tests is under current research and will be addressed in a separate work.

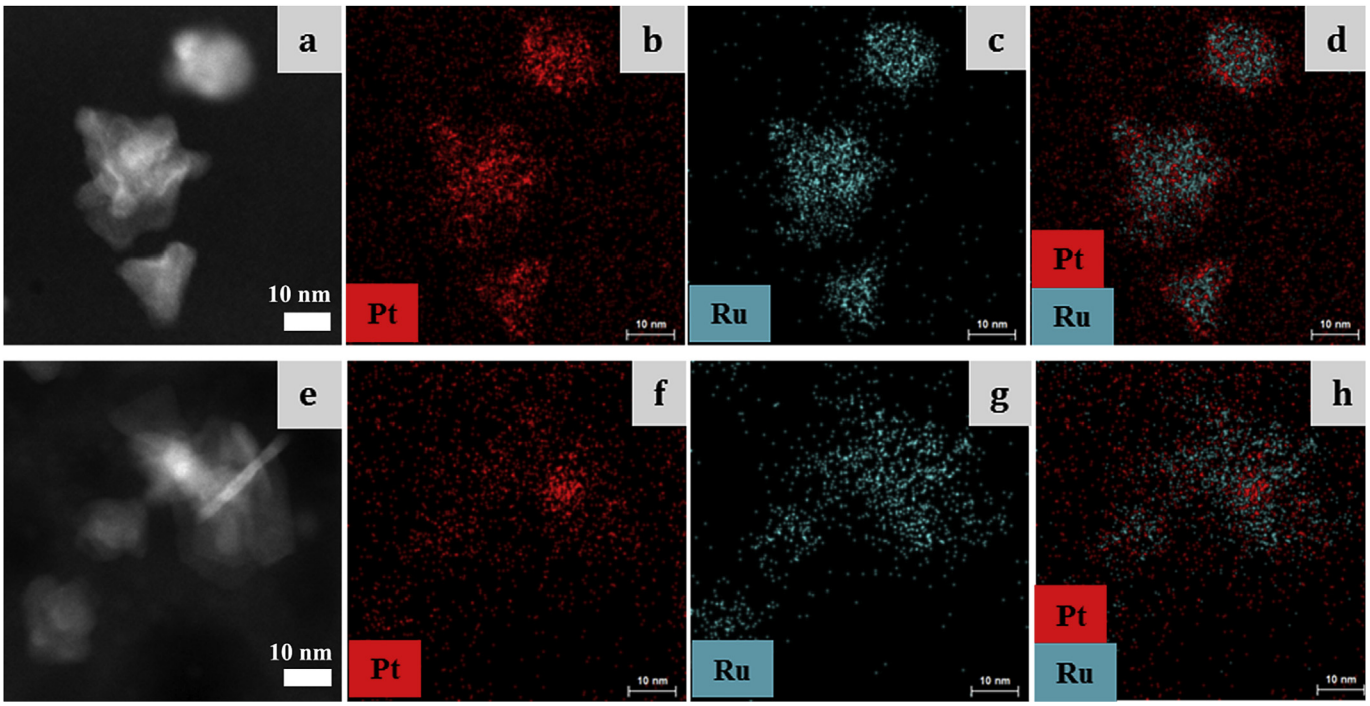

Fig. 5. EDX map of nanoparticles in the membrane of the operated MEA_t1 and MEA_t2. Insight into the membrane of MEA_t1: a) HRSTEM image, b) Pt distribution in red, c) Ru distribution in blue, d) overlay of Pt and Ru distribution. Insight into the membrane of MEA_t2: e) HRSTEM micrograph; f) Pt distribution in red; g) Ru distribution in blue; h) overlay of Pt and Ru distribution. (For interpretation of the references to colour in this figure legend, the reader is referred to the web version of this article.)

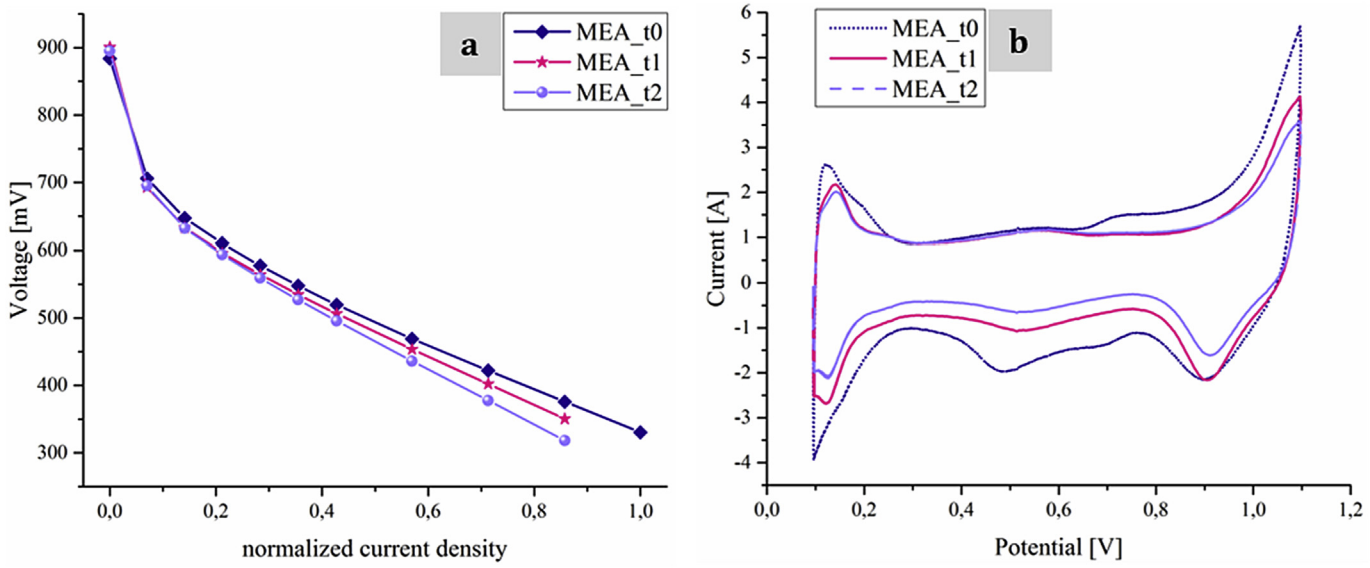

Fig. 6. Results of electrochemical measurements: a) Polarization curves of MEA_t0, MEA_t1 and MEA_t2; b) Cyclic voltammetry (CV) of all MEAs.

3.5. Electrochemical analysis

In Fig. 6a, polarization curves of the MEAs are displayed. During the acquisition, the anode was fed with synthetic reformat and the operation temperature was 160 °C. In all three MEAs, the open circuit voltage (OCV) stays constant within the error range around 900 mV. This indicates that no short circuit or gas leakage is occurring during fuel cell operation which conforms to the results from SEM analysis presented in section 3.1. With increasing operational time the internal resistance of the MEAs increase as can be seen in the ohmic part of the polarization curves.

The extent of the accessible surface area of the Pt NPs on the HSAC support in the cathode CLs of the MEAs was measured by the hydrogen underpotential deposition (H_{UPD}) charge in cyclic voltammetry experiments. The obtained curves, as displayed in Fig. 6b, are comparable in shape. The first peak at low potential and positive current arises from desorption of adsorbed H_2 and is therefore used for the calculation of the electrochemical surface area (ECSA). The other peaks are related to Pt oxidation, Pt-*O*-reduction and hydrogen adsorption and are not considered for the ECSA

calculation. With excess of H_3PO_4 the Pt (111) and Pt (100) surfaces are blocked by PO_4^{3-} anions. Therefore no designated Pt-H features on the different surfaces can be observed. This is also described by He et al. [23] In Table 5, the ECSAs of the three investigated MEAs are summarized.

Compared to the reference MEA_t0 which has not been operated, a gradual decrease of the ECSA in MEA_t1 and MEA_t2 has been observed. The ECSA of Pt in the cathode CL of MEA_t0 was calculated to be 122 ± 6 cm^2/mg. After the first time interval of fuel cell operation (MEA_t1) the accessible surface area of Pt was found to be 81 cm^2/mg and after twice the operation time (MEA_t2), 71 cm^2/mg. This result is the consequence of several reasons: As presented in the supplementary Fig. S3, the size of the Pt nanoparticles in the cathode catalyst layer increases with fuel cell operation time and, accordingly, the overall catalyst surface area decreases. Additionally, a small part of Pt was found to diffuse into the membrane making it inaccessible for the cathode's oxygen reduction reaction and lowering the ECSA value. Also, thinning of the cathode CL due to oxidation of the carbon support (SEM analysis, Fig. 1) causes the Pt catalyst NPs to form agglomerates or detach from the electrode. The loss in ECSA during the first operation time interval (MEA_t1) represents about one third of the accessible catalyst area. Nevertheless, the losses after another time interval (MEA_t2) of operation are only about 10%. This shows that the first thousands of operating hours have the highest impact on particles' coarsening.

Fig. 7 shows the Nyquist plots obtained by electrochemical impedance spectroscopy (EIS). The diameters of the semicircles at medium frequencies are dominated by the activity of the cathode catalyst for the ORR. The formation of a semicircle at high frequencies is indicative for a decrease of anode catalyst activity with increased operation time. In MEA_t0, the resistances measured are slightly higher than in MEA_t1, indicating a better performance after the first interval of fuel cell operation. This is related to the fact that the test for MEA_t0 was performed directly after MEA production. During the conditioning phase of the fuel cell, the H_3PO_4 is redistributed and the performance of the fuel cell is improving. The resistances in MEA_t2 increased compared to MEA_t0 and MEA_t1. This can be explained by the loss of carbon material and a decreased accessible catalyst surface area due to Ostwald ripening and nanoparticle dissolution. We found this result to be in good agreement with our SEM and TEM analysis in section 3.1–3.4. The ionic membrane resistance was found to stay constant within the error range.

4. Discussion

The present work reveals micro- and nanoscale degradation processes that occur during long-term operation of HT-PEMFCs. SEM investigation of cross-sections of the three investigated MEAs – where MEA_t0 was not operated while MEA_t1 and MEA_t2 were operated for specific time intervals t1 and t2 – revealed an operation-related thickness decrease of the anode and

Table 5
Electrochemical surface area (ECSA) of the Pt catalyst at the cathode of all MEAs obtained from the hydrogen underpotential deposition (H_{UPD}) charge from the CV experiments.

	ECSA (cm^2 Pt/mg Pt)
MEA_t0	122 ± 6
MEA_t1	81 ± 4
MEA_t2	71 ± 4

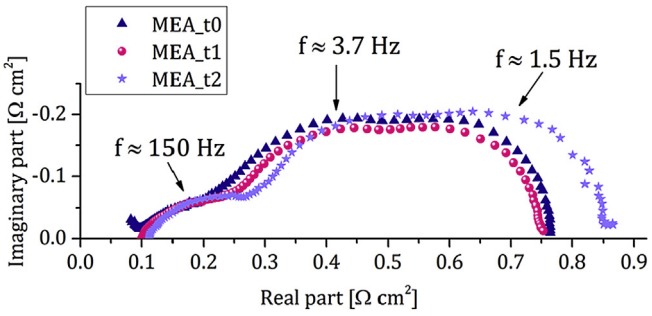

Fig. 7. Nyquist plots of EIS measurements of all investigated MEAs.

cathode catalyst layers and the membrane. This effect is strongest for the membrane and the cathode CL and almost negligible for the anode CL. The membrane, which is composed of the organic polymer polybenzimidazole, is known to be susceptible to weight loss during fuel cell operation and a lot of effort has been, and is still being put in to increase its stability further [17,21,24,25]. Also, carbon corrosion in the electrochemical environment of the fuel cell during operation is a known and well-documented process in literature and many research activities are focusing on overcoming this issue by either stabilizing the carbon support or replacing it by other promising materials [26]. Nevertheless, even though we observe a thickness decrease of our MEA components, our system does not experience a catastrophic failure. All MEA specific components like the membrane, anodic and cathodic catalyst layers, microporous layers and gas diffusion layers were investigated in the SEM to a great extent and over large areas. No holes could be detected in any membrane section, suggesting that neither a short circuit nor a gas leak was occurring. The catalyst layers reveal holes at regular intervals, which is due to the drying process of the electrodes during their fabrication and partly due to operation-related loss of the carbon support.

The formation of a Pt band has been discussed in literature to a great extent for Nafion membranes of PEMFCs. Most authors agree in their explanations on how Pt catalyst dissolution and precipitation take place, why there is a band forming and where the band is located: A potential effect at the cathode side is proposed to account for the Pt particle dissolution while residual oxygen oxidizes the catalyst, resulting in Pt^{z+} ions and Pt oxides which dissolve in water [10,13,27]. Diffusion of these ions and oxides takes place as a consequence of the concentration gradient between cathode and membrane [12], electro-osmotic drag and chemical diffusion [11,28]. Cross-leaked hydrogen stemming from the anode is supposed to reduce these Pt^{z+} ions and oxides in the membrane to metallic Pt and itself is forming protons. The mechanism described is assumed to be a repetitive one. Following this explanation, the final position of the Pt band in the membrane depends on the partial pressures of oxygen and hydrogen, and the gas permeability of the membrane [12–14,29–31]. Zhang et al. [22] present a theoretical model and experimental proof that the exact location of the Pt band in the membrane is in the position where the ratio of the molar flux of H_2 vs. O_2 equals 2/1. The authors state this to be the critical value of H_2 excess to create a reducing environment that prevents a repeated dissolution of the previously redeposited catalyst. The amount of dissolved Pt depends on the operation time, rather than the potential conditions [32]. Only a few reports can be found in which Pt dissolution at the anode is described [13,15]. Moreover, many authors claim an inhibition of anodic Pt dissolution due to the low anodic potential compared to the Pt redox potential, and also that the anodic hydrogen oversupply reduces all eventually formed Pt-oxides [10,27]. However,

Xie et al. pointed out in their work that this only accounts for Pt bulk material. Since the catalyst normally used in PEMFCs is in the form of nanoparticles, which are designed to exhibit a high surface area, their electrochemical thermodynamics differ from Pt bulk characteristics. This was also later confirmed by Tang et al. [33]. Additionally elevated operation temperatures promote dissolution.

Several research works analyzing the activity and stability of Ru compared to RuO_2 and Pt can be found in literature [19,34,35]. The results show a relatively low stability of Ru in an electrochemical environment. On the other hand, a good activity of Ru and an improved performance when using the Pt/Ru-C system in PEMFCs and HT-PEMFCs was found.

Henry et al. [19] presented a detailed TEM study of Pt-Ru precipitates in the membrane of aged PEMFCs which were operated at 75 °C: Similar to the work in hand, the authors observed a band in the membrane formed by Pt/Ru particles adjacent to the cathode catalyst layer. The authors describe the shape of these precipitates as flower- and star-like. Size and elemental distribution of these catalyst particles are different than the ones presented here. The authors found Pt-core, Ru-shell polycrystalline particles in the membrane and state that their elemental distribution is a result of their formation process: After operation-related dissolution and migration of Pt from the cathode CL and Ru from the anode CL, the dissolved Pt ions are first reduced by crossover hydrogen and accordingly form Pt nanoparticles. These nanoparticles are then proposed to catalyze the reduction of dissolved Ru which precipitates around them, thus forming the observed core-shell structures.

The nano- and micrometer scale observations in our fuel cell system slightly differ from the one described above. The differences can be attributed to the fact, that in the present work HT-PEMFCs are studied with an operation temperature of 160 °C. A schematic drawing of the processes that take place in our system is presented in Fig. 8. Unlike Henry et al., we found both Pt and Ru dissolving from the anode side and, similar to their work, we also found a small amount of Pt dissolving from the cathode side. These elements firstly form spherical shaped nanoparticles with a size of a few nanometers in the membrane area close to the anode and cathode catalyst layers respectively. During fuel cell operation, a repetitive dissolution, migration and precipitation of the catalyst seems to take place. The Pt/Ru catalyst stemming from the anode side was found to form 14–16 nm sized, starlike shaped particles in the membrane area adjacent to the cathode CL. The elemental distribution within these particles is homogeneous after the first time interval (MEA_t1) of fuel cell operation. After the second operation time interval (MEA_t2) a Pt accumulation within the observed particles was found while Ru is distributed uniformly. It was also observed that, apart from the Pt rich region, the particles embedded in the membrane of MEA_t2 are composed of facetted, overlapping discs. The diffraction patterns obtained from these structures in MEA_t1 and MEA_t2 reveal that the Pt/Ru nanoparticles adopted the hcp lattice due to the high Ru content. The diffusion direction of the anode catalyst is in accordance with the protons constantly forming at the fuel cell's anode and travelling to the cathode side. Pt catalyst dissolution and migration from the cathode CL into the membrane was detected as well. Pt and Pt/Ru from the cathode and anode catalyst layers diffuse into the membrane and form nanoparticles which accumulate into a band. The distance between this band and the cathode catalyst layer was found to decrease from 2.3 ± 0.2 μm (MEA_t1) to 0.4 ± 0.1 μm (MEA_t2) with ongoing fuel cell operation time. Since the average thickness decrease of the whole membrane after the operated time intervals of the investigated MEAs is larger than the difference of 1.9 μm (as was found by SEM analysis), the position of the band in the membrane is determined by other parameters (than the thickness). Rather, as mentioned before, it is dependent on the ratio of the molar flux of H_2/O_2 which was found by Zhang et al. to be 2/1 at the position of the band and the gas permeability characteristics of the membrane [22]. It is also worth mentioning that according to the authors the position of the band is independent of the membrane thickness. We believe that the band of catalyst nanoparticles in the membrane might be beneficial for the fuel cell's performance. The catalyst particles in the membrane act as an active filter for cross-leaking O_2 and H_2. O_2 reacts with metallic Pt or Ru to form the related oxides, while water is formed in the presence of H_2 and metallic Pt or Ru is redeposited. In the absence of the catalyst material in the membrane, H_2 and O_2 would be free to migrate all the way to their counter electrode in the MEA and, while doing so, omit the key processes of the fuel cell operation steps. Our results have shown that the relative position of the band in relation to the decreasing membrane thickness changes with ongoing fuel

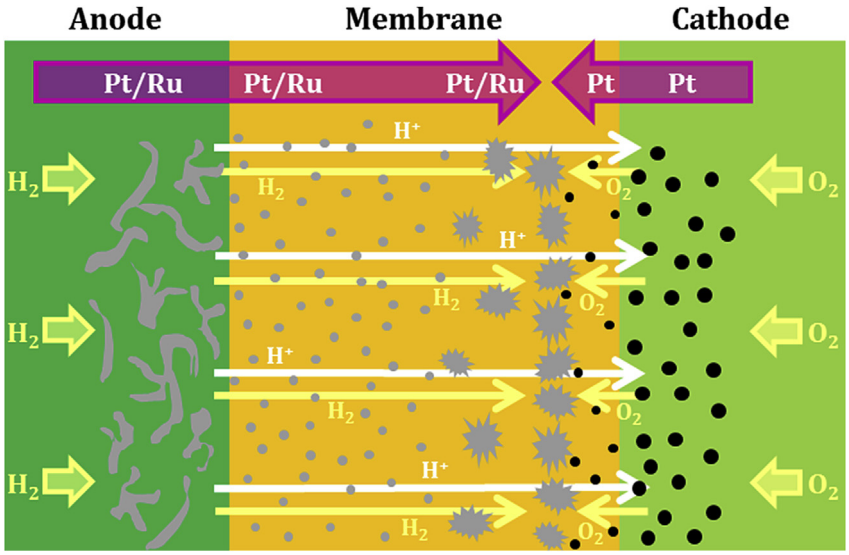

Fig. 8. Schematic drawing of the nano- and micrometer scale processes that take place during fuel cell operation. Unintentional H_2 and O_2 diffusion into the membrane occurs as outlined by the yellow arrows. Instead, only diffusion of H^+ (indicated by white arrows) is desired. For simplification, the reduction of O_2 at the cathode is not drawn. (For interpretation of the references to colour in this figure legend, the reader is referred to the web version of this article.)

cell operation time. This indicates that the O_2 and/or H_2 permeability of the PBI-based material has changed due to degradation. This can be minimized by chemical and/or mechanical strengthening of the membrane and most efficiently by using a PBI with a small distribution of the polymer chain length [25].

Ru crossover from the anode through the membrane into the cathode side has been reported previously, not only in PEMFCs, but also in direct methanol fuel cells (DMFCs) where Ru was detected in the cathode catalyst layer after fuel cell operation [36,37]. The presence of Ru at the cathode side is known to inhibit the oxygen reduction reaction kinetics which are already among the limiting factors in fuel cell performance [38]. In our case the catalyst material stays in the membrane. As long as this status is preserved, a catastrophic failure of the fuel cells is prevented. We also found that the amount of Ru and Pt dissolving at the beginning of fuel cell operation is higher than that with ongoing operation time. This may be because smaller particles in the anode dissolve at an early state while bigger agglomerates of Pt/Ru particles are more stable. Furthermore, most of the catalyst material is still present at the anode side and only a comparably small amount of catalyst dissolved and diffused into the membrane. Nevertheless, these stability issues are not to be neglected and a lot of efforts are made to prevent catalyst dissolution at all and improve the fuel cells' performance.

5. Conclusion

The work in hand presents an in-depth study of nano- and micrometer scale processes that take place during operation of high-temperature polymer-electrolyte-membrane fuel cells. As catalyst material, Pt was used at the cathode side and a mixture of Pt and Ru at the anode side to counteract CO poisoning effects. Altogether, three MEAs were investigated: MEA_t0 was not operated while MEA_t1 and MEA_t2 were operated for specific time intervals. MEA_t2 was operated for about twice as long as MEA_t1. SEM investigation reveals a thinning of all MEA components with ongoing fuel cell operation time. Since the operation conditions at the cathode side are harsher than at the anode side, mainly due to the presence of oxygen, the cathode was found to be more susceptible to corrosion than the anode. TEM investigation of the membrane/cathode and membrane/anode transition areas revealed a band of Pt and Pt/Ru nanoparticles in the membrane area adjacent to the cathode catalyst layer. Additionally, nanoparticles were detected in the membrane area between the anode catalyst layer and the band. The catalyst material forming the band originates from both catalyst layers. The band-forming particles containing 71–82 atom% Ru on average, depending on the operation time, exhibit a starlike shape with a size distribution of 14–16 nm and possess a hexagonal crystal structure. Additionally, a small amount of nearly spherical Pt nanoparticles was observed. The position of the band within the membrane is determined by the partial pressures of oxygen and hydrogen and by the gas permeability of the membrane. Its location is not permanent since the thinning of the membrane gives a stronger effect than the distance decrease between band and cathode catalyst layer. Instead, its position is dependent on the 2/1 ratio of the molar flux of H_2 and O_2. Even though the catalyst material in the membrane is inactive for the fuel cell's ORR or HOR, the material does act as an active barrier for cross-leaking H_2 and O_2; this might even benefit the fuel cell's performance.

Acknowledgement

Financial support from the German Federal Ministry for Economy and Technology (KF2001502ZG4) within the program ZIM-KOOP is gratefully acknowledged. The authors thank Martin Palm and Frank Stein for their help with the Pt/Ru phase diagram and Scott Schmeits for his technical support and guidance. Anna Frank is gratefully acknowledged for support of EDX measurements.

Appendix A. Supplementary data

Supplementary data related to this article can be found at http://dx.doi.org/10.1016/j.jpowsour.2017.08.042.

References

[1] P.P. Lopes, K.S. Freitas, E.A. Ticianelli, Electrocatalysis 1 (2010) 200–212.
[2] S.M.M. Ehteshami, S.H. Chan, Electrochimica Acta 93 (2013) 334–345.
[3] L.G.S. Pereira, V.A. Paganin, E.A. Ticianelli, Electrochimica Acta 54 (2009) 1992–1998.
[4] J.J. Linares, T.A. Rocha, S. Zignani, V.A. Paganin, E.R. Gonzalez, Int. J. Hydrogen Energ 38 (2013) 620–630.
[5] O.A. Petrii, J. Solid State Electrochem 12 (2008) 609–642.
[6] T.R. Ralph, M.P. Hogarth, Platin. Met. Rev. 46 (2002) 117–135.
[7] A.E. Russell, S.C. Ball, S. Maniguet, D. Thompsett, J. Power Sources 171 (2007) 72–78.
[8] P.P. Lopes, E.A. Ticianelli, J. Electroanal. Chem. 644 (2010) 110–116.
[9] C. Takei, K. Kakinuma, K. Kawashima, K. Tashiro, M. Watanabe, M. Uchida, J. Power Sources 324 (2016) 729–737.
[10] W. Bi, G.E. Gray, T.F. Fuller, Electrochem. Solid-State Lett. 10 (2007) B101–B104.
[11] S. Zhang, X.-Z. Yuan, J.N.C. Hin, H. Wang, K.A. Friedrich, M. Schulze, J. Power Sources 194 (2009) 588–600.
[12] A. Ohma, S. Suga, S. Yamamoto, K. Shinohara, ECS Trans. 3 (2006) 519–529.
[13] L. Kim, C.G. Chung, Y.W. Sung, J.S. Chung, J. Power Sources 183 (2008) 524–532.
[14] K. Yasuda, A. Taniguchi, T. Akita, T. Ioroi, Z. Siroma, Phys. Chem. Chem. Phys. 8 (2006) 746–752.
[15] J. Xie, D.L. Wood, K.L. More, P. Atanassov, R.L. Borup, J. Electrochem. Soc. 152 (2005) A1011–A1020.
[16] M. Rau, A. Niedergesäß, C. Cremers, S. Alfaro, T. Steenberg, H.A. Hjuler, Fuel Cells 16 (2016) 577–583 n/a-n/a.
[17] T. Ossiander, M. Perchthaler, C. Heinzl, C. Scheu, J. Power Sources 267 (2014) 323–328.
[18] L.A. Giannuzzi, F.A. Stevie, Micron 30 (1999) 197–204.
[19] P.A. Henry, L. Guétaz, N. Pélissier, P.-A. Jacques, S. Escribano, J. Power Sources 275 (2015) 312–321.
[20] J.M. Hutchinson, Platin. Met. Rev. 16 (1972) 88–90.
[21] T. Ossiander, C. Heinzl, S. Gleich, F. Schönberger, P. Völk, M. Welsch, C. Scheu, J. Membr. Sci. 454 (2014) 12–19.
[22] J. Zhang, B.A. Litteer, W. Gu, H. Liu, H.A. Gasteiger, J. Electrochem. Soc. 154 (2007) B1006–B1011.
[23] Q. He, X. Yang, W. Chen, S. Mukerjee, B. Koel, S. Chen, Phys. Chem. Chem. Phys. 12 (2010) 12544–12555.
[24] C. Heinzl, T. Ossiander, S. Gleich, C. Scheu, J. Membr. Sci. 478 (2015) 65–74.
[25] T. Ossiander, M. Perchthaler, C. Heinzl, F. Schönberger, P. Völk, M. Welsch, A. Chromik, V. Hacker, C. Scheu, J. Membr. Sci. 509 (2016) 27–35.
[26] C. Heinzl, K.A. Hengge, M. Perchthaler, V. Hacker, C. Scheu, J. Electrochem. Soc. 162 (2015) F280–F290.
[27] C.G. Chung, L. Kim, Y.W. Sung, J. Lee, J.S. Chung, Int. J. Hydrogen Energ 34 (2009) 8974–8981.
[28] E. Guilminot, A. Corcella, F. Charlot, F. Maillard, M. Chatenet, J. Electrochem. Soc. 154 (2007) B96–B105.
[29] F. Ettingshausen, J. Kleemann, M. Michel, M. Quintus, H. Fuess, C. Roth, J. Power Sources 194 (2009) 899–907.
[30] F. Ettingshausen, J. Kleemann, A. Marcu, G. Toth, H. Fuess, C. Roth, Fuel Cells 11 (2011) 238–245.
[31] T.T.H. Cheng, E. Rogers, A.P. Young, S. Ye, V. Colbow, S. Wessel, J. Power Sources 196 (2011) 7985–7988.
[32] M. Zhao, W. Shi, B. Wu, W. Liu, J. Liu, D. Xing, Y. Yao, Z. Hou, P. Ming, J. Gu, Z. Zou, Int. J. Hydrogen Energ 39 (2014) 13725–13737.
[33] L. Tang, B. Han, K. Persson, C. Friesen, T. He, K. Sieradzki, G. Ceder, J. Am. Chem. Soc. 132 (2010) 596–600.
[34] S.M. Andersen, L. Grahl-Madsen, E.M. Skou, Solid State Ionics 192 (2011) 602–606.
[35] S. Cherevko, S. Geiger, O. Kasian, N. Kulyk, J.-P. Grote, A. Savan, B.R. Shrestha, S. Merzlikin, B. Breitbach, A. Ludwig, K.J.J. Mayrhofer, Catal. Today 262 (2016) 170–180.
[36] P. Piela, C. Eickes, E. Brosha, F. Garzon, P. Zelenay, J. Electrochem. Soc. 151 (2004) A2053–A2059.
[37] W. Chen, G. Sun, J. Guo, X. Zhao, S. Yan, J. Tian, S. Tang, Z. Zhou, Q. Xin, Electrochimica Acta 51 (2006) 2391–2399.
[38] H.A. Gasteiger, J.E. Panels, S.G. Yan, J. Power Sources 127 (2004) 162–171.